

See discussions, stats, and author profiles for this publication at: <https://www.researchgate.net/publication/221981403>

Directional Scattering and Hydrogen Sensing by Bimetallic Pd-Au Nanoantennas

ARTICLE *in* NANO LETTERS · MARCH 2012

Impact Factor: 13.59 · DOI: 10.1021/nl300558h · Source: PubMed

CITATIONS

43

READS

102

4 AUTHORS, INCLUDING:



[Timur Shegai](#)

Chalmers University of Technology

29 PUBLICATIONS 885 CITATIONS

[SEE PROFILE](#)



[Christoph Langhammer](#)

Chalmers University of Technology

63 PUBLICATIONS 1,622 CITATIONS

[SEE PROFILE](#)

Directional Scattering and Hydrogen Sensing by Bimetallic Pd–Au Nanoantennas

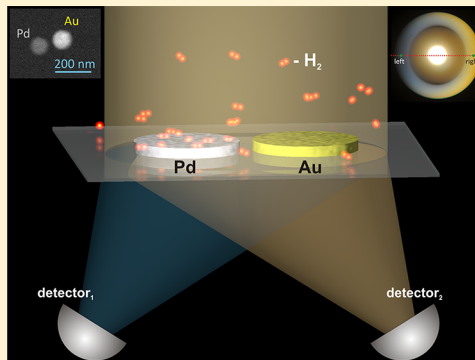
Timur Shegai,[†] Peter Johansson,^{†,§} Christoph Langhammer,[†] and Mikael Käll^{†,*}

[†]Department of Applied Physics, Chalmers University of Technology, 412 96 Göteborg, Sweden

[§]School of Science and Technology, Örebro University, 701 82 Örebro, Sweden

Supporting Information

ABSTRACT: Nanoplasmonic sensing is typically based on quantification of changes in optical extinction or scattering spectra. Here we explore the possibility of facile self-referenced hydrogen sensing based on angle-resolved spectroscopy. We found that heterodimers built from closely spaced gold and palladium nanodisks exhibit pronounced directional scattering, that is, for particular wavelengths, much more light is scattered toward the Au than toward the Pd particle in a dimer. The effect is due to optical phase shifts associated with the material asymmetry and therefore highly sensitive to changes in the permittivity of Pd induced by hydrogen loading. In a wider perspective, the results suggest that directional scattering from bimetallic antennas, and material asymmetry in general, may offer many new routes toward novel nanophotonic sensing schemes.



KEYWORDS: *Nanoantenna, plasmonic sensing, hydrogen sensing, directional emission, material asymmetry, palladium nanoparticles*

The ability to measure hydrogen concentrations is important in many industrial processes and will become a major safety concern if the development of fuel cell technology leads to widespread use of hydrogen as a carbon-free fuel for vehicles.¹ Specifically, the danger of using hydrogen is related to the high risk of explosion if hydrogen gas is mixed with air at concentrations above 4%. However, safety issues will always arise when hydrogen is used or produced, regardless of the particular application. This motivates the development of highly sensitive, cheap, and robust hydrogen sensors.

Pd is used as the active element in many state-of-the-art hydrogen detection technologies because of its thermodynamically suitable and fully reversible hydride formation properties under ambient conditions.² The conductivity and dielectric properties of palladium change on hydrogen exposure,³ which makes it well-suited for both electrical^{4,5} and optical^{6–11} sensing schemes. One particular aspect in favor of the latter is the possibility for remote contact-free readout, which increases the inherent safety of the sensor as no electric sparks can be generated.

Optical sensors that utilize the plasmonic properties of metal nanostructures,^{12,13} so-called localized surface plasmon resonance (LSPR) sensors, are of high current interest in, for example, label-free bioanalysis.^{14,15} The transduction mechanism of spectroscopic LSPR sensing is based on detecting changes in the plasmon resonance condition caused by adsorption of target species in the vicinity of the metal nanoparticle(s). LSPR sensing thus typically focuses on spectral measurements of sometimes tiny changes in the plasmon resonance peak position or intensity.^{16–18} This measurement

methodology has also been employed in the recent development of nanoplasmonic hydrogen sensors based on Pd–Au composite nanostructures, including the recent reports on measurements of individual isolated nanostructures.^{6,7,10} In contrast, traditional surface plasmon resonance (SPR) sensors based on macroscopic metal films usually utilize single-wavelength angle-resolved detection schemes,¹⁹ which can take full advantage of the wide availability of cheap and robust monochromatic laser sources and simple single channel detectors. A similar approach to LSPR hydrogen sensing obviously requires nanostructures that exhibit some kind of H₂-dependent directionality effect in their spectral emission or excitation characteristics.

In this Letter, we describe how nanoantennas in the form of closely spaced Pd and Au nanodisks can be used for directional sensing of hydrogen. As a proof-of-principle, we demonstrate single-wavelength self-referenced measurements of H₂ across the α – β transition in the Pd–H phase diagram. The directionality effect that we utilize has the same origin as the color routing process recently reported for Au–Ag heterodimers and is due to internal optical phase shifts associated with the bimetallic nature of an individual nanoantenna.²⁰ The fact that directional Pd–Au dimer antennas can be easily fabricated over extensive areas using simple colloidal lithography indicates the potential for real-life sensing applications.

Received: February 9, 2012

Revised: March 20, 2012

Published: March 26, 2012

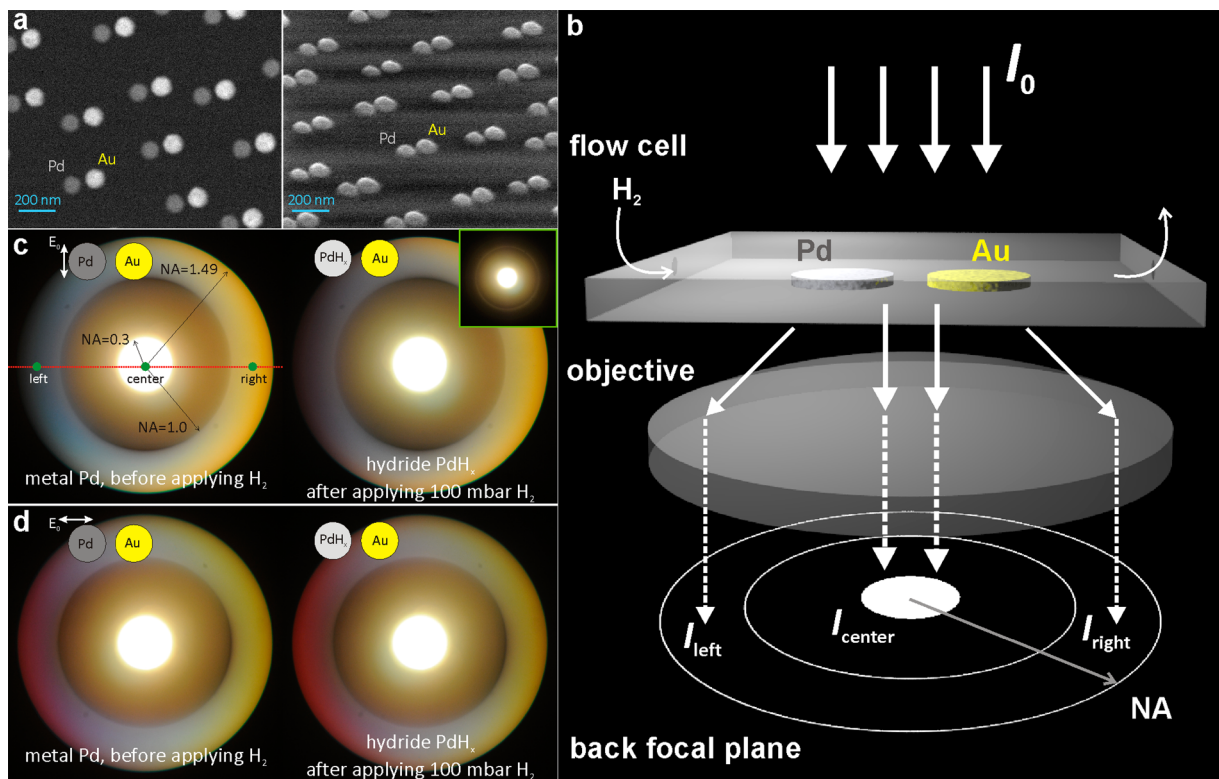


Figure 1. (a) SEM images of Pd–Au dimers: top view (left) and 45° inclined view (right). (b) Schematic illustration of the measurement setup. Angle-resolved scattering spectra can be collected by positioning a fiber coupled to a spectrometer at the desired location in a Fourier plane conjugate to the back-focal plane of the objective. (c) Fourier color images obtained for incident polarization perpendicular to the dimer axis before (left) and after (right) applying a hydrogen partial pressure of 100 mbar. The inset shows a Fourier image of the straylight background obtained under the same illumination conditions. (d) Same as in (c) but for polarization parallel to the dimer axis.

Basic Principle of Directional Emission from Bimetallic Dimers. The directional spectrum of a Pd–Au dimer is, in a first approximation, determined by the interparticle distance and the wavelength-dependent polarizabilities of the individual Pd and Au nanoparticles. Consider two dipoles positioned on the x -axis at $x_{\text{Pd}} = 0$ and $x_{\text{Au}} = L$, respectively, with their dipole moments pointing in the y -direction. The scattered intensity in the xz -plane is then proportional to $p_{\text{Au}}^2 + p_{\text{Pd}}^2 + 2p_{\text{Au}}p_{\text{Pd}} \cos(k_x L - \Delta\phi)$, where k_x is the wave vector component along the dimer axis, L is the interdipole distance, $p_{\text{Au(Pd)}}$ are the magnitudes of the Au(Pd) dipoles, and $\Delta\phi = \phi_{\text{Au}} - \phi_{\text{Pd}}$ is the internal phase difference between the two dipoles, as determined by their resonance properties. The first two terms in this expression correspond to scattering from the individual Au and Pd dipoles, whereas the third term describes their interference, which is the origin of the directional emission effect. The directions along the antenna axis, which correspond to forward ($k_x = k$) and backward ($k_x = -k$) emission, are the most interesting for this study. Scattering in the forward direction reaches a maximum when $kL - \Delta\phi = 2\pi m$ (m is an integer) and reaches a minimum in the backward direction when $-kL - \Delta\phi = \pi + 2\pi m$. Thus, in an ideal situation, emission of two dipoles can be completely nullified in one direction, while having a maximum in the other, provided that $p_{\text{Pd}} = p_{\text{Au}}$, $\Delta\phi = \pi/2$, and $L = \lambda/4$.

Samples and Measurement Strategy. With the discussion above in mind, we fabricated planar dimer antennas composed of closely positioned Au and Pd nanodisks on 1 in. SiO_2 microscope coverslips using hole-mask colloidal lithography (HCL)²¹ using sequential deposition of Pd and Au in

alternating 10 nm steps at angles of 25° and -25° off normal incidence, respectively. This hybrid bottom-up/top-down nanofabrication technique makes it possible to cover large areas (cm^2) with short-range ordered bimetallic dimers of identical orientation and material composition,^{20,21} see Figure 1a. The disk diameters ($D = 100$ nm) and thicknesses ($t = 30$ nm) were the same for the Pd and Au nanodisks, and the interparticle gap was $d = 25$ nm, as determined from scanning electron microscopy (SEM) image analysis. This means that the overall size of a single dimer antenna is $\sim 225 \times 100 \times 30 \text{ nm}^3$, which is subwavelength in all three spatial dimensions. The particular design parameters were chosen so as to give a strong spectral response for visible wavelengths.

A sketch of the hydrogen sensing experiments is shown in Figure 1b. The samples were positioned inside a stainless steel flow cell (volume $\approx 110 \mu\text{L}$) mounted on XY stage of an inverted microscope (Nikon Eclipse TE2000-E). A set of mass flow controllers (Bronckhorst low Δp) with different working ranges was used to set the desired concentration of hydrogen in the flow cell at a constant total gas flow of 150 mL/min (Ar was used as the carrier gas). The dimers were excited from above using linearly polarized white light produced by a halogen lamp and focused by a long working distance 10 \times numerical aperture (NA) = 0.3 objective that illuminated an area of about 100 μm in diameter. The elastically scattered and transmitted light was collected by an oil immersion objective with ultrahigh NA (60 \times , NA = 1.49 Nikon). The direction of the scattered radiation could be directly imaged in a plane that was conjugate to the objective's back focal plane (Fourier plane) using a charge-coupled device (CCD) camera.²⁰

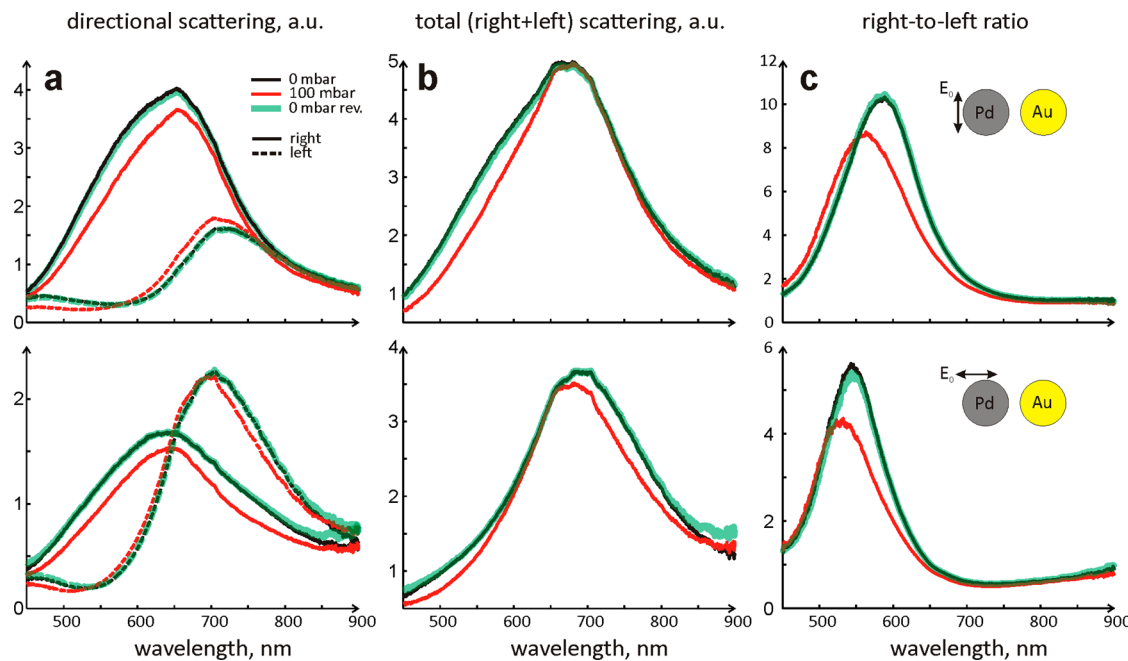


Figure 2. Spectral response to a change in hydrogen partial pressure from 0 mbar (black curves) to 100 mbar (red) and back to 0 mbar (green) for incident polarization perpendicular (upper three panels) and parallel to the dimer axis (lower three panels). (a) Scattering spectra collected from the right (full lines) and the left parts (dashed lines) of the Fourier plane. (b) Sums of the right and the left spectral channels. (c) Ratios between the right and the left spectral channels.

Experimental Results. Figure 1c,d illustrates the main observation for the case of the incident light being polarized perpendicular and parallel to the dimer axis, respectively. The pictures show Fourier images taken before H₂ exposure, i.e., samples are in a pure Ar atmosphere, and after applying a partial pressure of 100 mbar H₂ in Ar, corresponding to complete conversion of the Pd nanodisks to the hydride phase PdH_x (where x is the hydrogen concentration). The bright spot in the center of the Fourier plane comes from the directly transmitted light. The spot has a radius that corresponds to the NA of the illumination source (NA = 0.3), while the outer radius of the Fourier image is determined by the maximum NA of the collection objective (NA = 1.49). One also clearly sees a circle at NA = 1 that corresponds to the critical angle of the air–glass interface.

Looking at Figure 1c,d, one immediately notices the color asymmetry caused by the directional scattering process. The right parts of the Fourier planes, which correspond to scattering in the direction of the Au disks in the dimers, are yellowish, while the left sides are either reddish or bluish depending on the incident polarization. The images also reveal a change in color between the different hydrogenation states. In particular, the H₂-induced shift from bluish to purplish in left part of the Fourier image for the perpendicular polarization case could be easily seen by the bare eye. The color shifts occur within seconds when the hydrogen partial pressure is increased from 0 to 100 mbar at constant total gas flow rate (150 mL/min) and signal the transition from metallic Pd (with hydrogen in solid solution) into the Pd hydride (PdH_x) β -phase.^{2,22} We should point out that the effects seen in Figure 1c,d arise from the structural asymmetry of an individual dimer, even though the scattering is collected from several hundred individual nanoantennas, because the short-range translational order in the sample only causes a symmetric modification of the scattering pattern, that is, the left–right asymmetry that each individual

dimer generates is unaffected by interference between nearby dimers.

In order to quantify the observed color changes, we positioned a fiber probe coupled to a spectrometer at the ‘left’ and ‘right’ locations within the Fourier plane and measured the corresponding scattering spectra, see Figure 2a, as described in refs 20 and 23. Measurements were taken first at 0 mbar, then at 100 mbar, and finally again at 0 mbar H₂ partial pressure to check the reversibility of the signal. For the perpendicular polarization case, it is apparent that the dimers scatter significantly less light into the left than into the right channel over almost the full spectral range. For parallel polarization, there is instead a pronounced redistribution in spectral weight between the left and the right channels.

The data in Figure 2a clearly demonstrate that the Pd–Au dimers scatter light in a highly directional manner. We find this result quite remarkable in view of the fact that the particular Pd–Au dimer structure used has not been precisely optimized for maximum directionality. Moreover, we should point out that the data in Figure 2a contain a straylight background originating from diffraction on various imperfections within the optical path. This background contributes equally to the left and right spectra and therefore reduces the relative difference between the two channels. A Fourier image of the straylight background is shown in the inset of Figure 1c, while the question of background subtraction is discussed in the Straylight Subtraction Section. It is likely that optimized structures and an improved measurement configuration with reduced straylight would yield an even higher directionality contrast than shown in Figure 2.

Apart from spectra recorded in the right and left parts of the Fourier plane, Figure 2 shows the sum and the ratio of the two channels for each polarization. The former spectra are similar to what one would measure in an image plane of the sample, where all scattering angles covered by the collection optics

contribute to the signal. Note that the spectral changes induced by hydrogenation is slight in the “sum” spectra compared to the ratios, which differ by more than 20% in the yellow spectral region. This means that one, in this case, would lose sensitivity by “traditional” LSPR sensing based on angular averaging. However, as mentioned in the Introduction, one should work at a single wavelength to take full advantage of the possibilities for simpler experimental solutions arising with an angular response. As recently suggested by Evlyukhin et al.,²⁴ an additional advantage is that single wavelength operation is easy to combine with self-referenced measurements. In the present case, this simply means to measure the ratio between the left and the right detection channels rather than their individual absolute values. This approach can significantly improve the signal-to-noise ratio in the measurement by compensating for temporal illumination and detection fluctuations, as is the case in standard double-beam spectrophotometry.

Single-Wavelength Self-Referenced Directional Hydrogen Sensing. To verify the applicability of the proposed sensing strategy, we performed a proof-of-principle study at incrementally increasing hydrogen partial pressures across the so-called α - β phase transition in the Pd–H binary system. Measurements were made at 595 nm, which is close to the maximum in the spectral ratio for the perpendicular polarization, by inserting a 4 nm band-pass filter in the optical path. The scattered light was detected in the Fourier plane using a CCD chip as in Figure 1. However, we now binned a number of pixels in the left and right parts of the recorded Fourier images, as shown in Figure 3a. The integrated intensities in the two regions, which we call “detector₁” and “detector₂”, then emulate an actual two-detector sensor device, and their ratio can be used for facile self-referenced measurements. Figure 3b shows data obtained in this way as a function of increasing and decreasing hydrogen partial pressure. The obtained curve corresponds to a so-called pressure–concentration (p –C) isotherm and essentially maps the Pd–H phase diagram.² Two clear regions are prominent in the diagram. At low hydrogen partial pressures, hydrogen is dissolved as a solid solution in metallic Pd. This so-called α -phase is clearly identified as the region up to \sim 20 mbar in the optical p –C isotherm. The solid solution regime is then followed by a well-defined first-order transition to the so-called β -phase at a critical pressure of about 20 mbar.²⁵ The dielectric response of the β -phase is distinctly different from pure Pd, and this is the ultimate cause of the variation seen in Figure 4b. Further pressure increase beyond the α - β transition only causes small ratio changes, as the Pd nanodisks are now almost fully hydrogenated. Finally, we note the hysteresis loop between the hydrogen absorption and desorption branches of the isotherm. The hysteresis is caused by memory effects associated with lattice strains induced by the volume expansion that occurs during the α - β transition. Overall, there is an excellent agreement between the data shown in Figure 3b and previous results based on traditional nanoplasmonic sensing.²²

Electrodynamics Simulations. To obtain more fundamental insight into the physics of the directional scattering phenomenon, we performed electrodynamics simulations of supported Pd–Au dimers in vacuum using the Green’s function method for layered systems.^{26,27} The calculations were made using cubic mesh elements of side length 2.5 nm. The wavelength-dependent dielectric constants for Au and Pd were taken from refs 28 and 29, respectively, the refractive index of the glass substrate was set to $n = 1.5$, and the geometrical

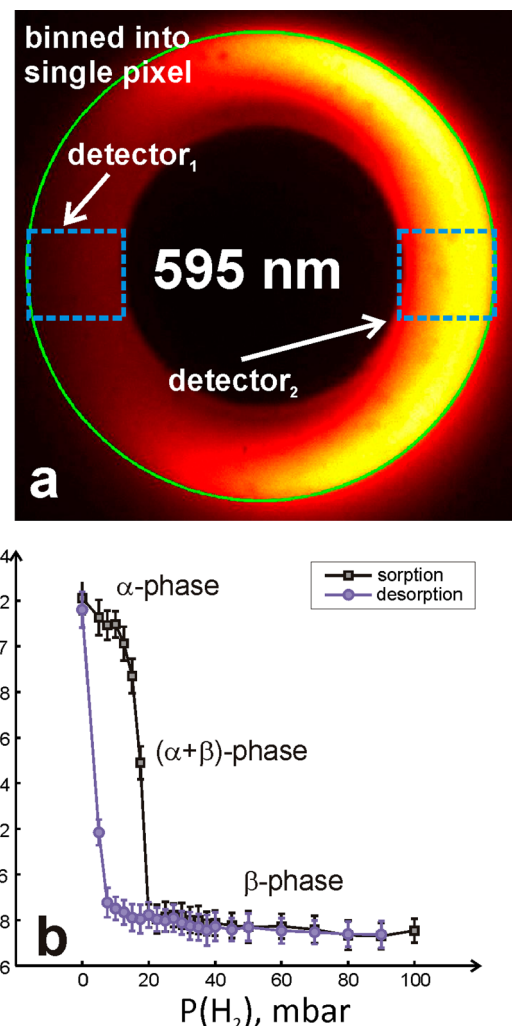


Figure 3. Proof-of-principle single-wavelength self-referenced hydrogen sensing. (a) A Fourier image obtained using 595 ± 2 nm excitation polarized perpendicular to the dimer axis. Areas surrounded with blue dashed rectangles were binned into a single pixel to emulate the two-detector measurements setup. (b) Ratio between intensities measured in detector₂ and detector₁ when increasing (squares) and decreasing (circles) the hydrogen partial pressure. Error bars show standard deviations over 30 repeated measurements.

parameters were obtained from the SEM image in Figure 1a, i.e., $D_{\text{Au}} = D_{\text{Pd}} = 100$ nm, $d = 25$ nm, and $t = 30$ nm.

Figure 4a shows scattering spectra integrated over all emission directions for the parallel and perpendicular polarization configurations. A spectral peak dominated by the LSPR of the gold disk is prominent at around 640 nm for both polarizations. The Pd disk is a much weaker scatterer, and its plasmon is broader and blue-shifted compared to the Au disk.³⁰ Hence, it is not easily discernible as a well-defined peak in the scattering spectra. For the parallel polarization case, the Au LSPR peak is slightly broader and shifted to the red compared to the perpendicular case because of the stronger near-field coupling to the Pd disk. Experimental scattering spectra recorded at 0 mbar hydrogen pressure are shown in Figure 2b for comparison. Although the experimental and simulated spectra do not fully agree in terms of peak positions, there is a qualitative agreement in terms of spectral shift between the two polarization configurations. The considerable broadening of the experimental spectra is mainly due to the polycrystalline nature

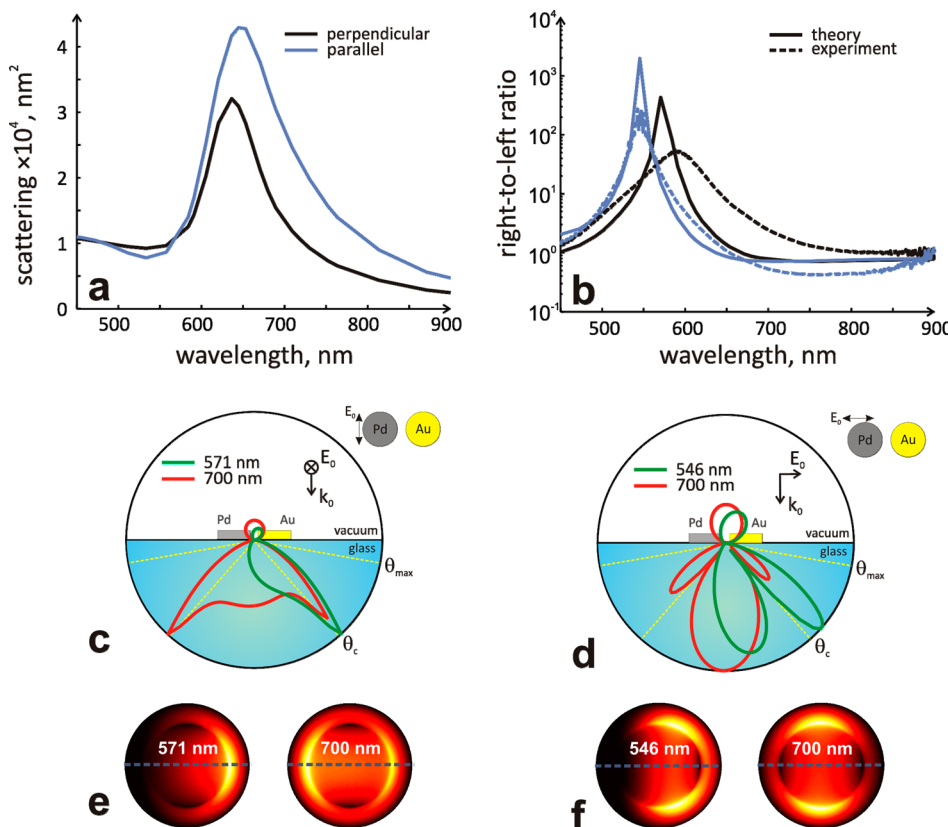


Figure 4. Electrodynamics simulations of directional scattering from a Pd–Au dimer antenna. (a) All-angle integrated scattering spectra for incident light polarized perpendicular (black) and parallel (blue) to the dimer axis. (b) Spectral ratios between light scattered toward the right and the left, as described in the main text. Full (dashed) lines correspond to theory (experiment). A straylight background was subtracted in the case of the experimental ratios. Note the logarithmic scale. (c,d) Scattering polar plots for perpendicular (c) and parallel (d) polarizations. The lower halfspace corresponds to glass and the upper halfspace to vacuum. Yellow dashed lines mark the critical angle and maximum collection angle in the experiments. (e,f) Calculated Fourier images for light emitted toward the glass substrate at representative wavelengths for perpendicular (e) and parallel (f) polarizations. The polar plots in (c,d) are taken along the gray dashed lines in the corresponding Fourier images.

of the nanodisks, which introduces additional plasmon damping due to grain boundaries and other imperfections that are not taken into account in the simulations. Experimental spectra are also widened due to inhomogeneous broadening.

Figure 4b shows calculated spectral ratios between the right (toward Au) and left (toward Pd) angular components of the scattering profiles. To mimic the experimental conditions, the scattering was integrated over an angular range roughly corresponding to that covered by the optical fiber used in the experiment ($1.2 < \text{NA} < 1.3$). The maximum ratios are obtained at 571 nm for the perpendicular and at 546 nm for the parallel polarization configuration, in good agreement with the experimental data. However, the actual calculated values obtained at these wavelengths are $I_r/I_l^{571\text{nm}} = 430$ and $I_r/I_l^{546\text{nm}} = 1984$. These numbers are significantly higher than the experimental results shown in Figures 2 and 3. The dominant cause for this discrepancy is the symmetric straylight background mentioned above. If we carefully subtract the background before taking the ratio, as described below, we obtain the experimental ratios shown in Figure 4b. These are in reasonably good agreement with the calculations. In addition, one may note that the ratio maxima appear to the blue of the respective maxima in the scattering spectra. As discussed in our earlier paper on color routing from Ag–Au antennas,²⁰ the directionality is typically highest when the optical phase shifts between the two antenna components is highest. In the present

case, this happens for wavelengths in between the Pd and Au LSPR's, that is, to the blue of the pronounced scattering peak.

Figure 4c,d shows radial scattering diagrams (polar plots) for representative wavelengths. We first note that there is significantly more light scattered toward glass than toward vacuum for both wavelengths shown. This is because an optically dense material (i.e., glass compared to vacuum, in this case) is able to “convert” evanescent waves above the interface to propagating ones below.^{23,31–34} This conversion is also the reason behind the pronounced intensity contrast between the allowed and forbidden zones, i.e., the regions inside and outside the critical angle of the air–glass interface. Second, one notes that the radiation pattern is almost completely symmetric at 700 nm for both polarization configurations. The reason is that this wavelength is to the red of both the Au and the Pd LSPR's and no internal phase shift exists that can cause directional scattering. The contrast between the 700 nm and the 571/546 nm diagrams, for which the optical phase difference and directionality is maximized, is dramatic. The difference is also obvious in the calculated Fourier images for light emitted toward the glass slide (Figure 4 e,f). It is also possible to extract the magnitudes and phases of the dipoles excited in the Pd and Au nanodisks from the Greens' function calculations, as shown in Figure S1 in the Supporting Information.

Straylight Subtraction. The symmetric background due to straylight, seen, e.g., in inset in Figure 1c, obviously reduces the ratio between the signals recorded in the right and the left

channels and therefore also the sensitivity of our hydrogen sensor. It is thus important to eliminate this background as much as possible in order to achieve the best sensor performance. Since the scattering centers responsible for the straylight are distributed symmetrically around the optical axis, without any particular phase retardation compared to the dimer antennas, one can in principle subtract the background. However, it is not possible to simply subtract the straylight Fourier image recorded without a sample in the optical path (the blank) from the raw sample data because straylight is generated all along the optical path, from light source to detector. In particular, that part of the straylight that is generated along the optical path between the sample and the detector can in principle be smaller with an optically dense sample in place than in a blank measurement. Indeed, we observed that subtracting the blank from the directional scattering data shown in Figure 2 resulted in negative intensity values for some wavelengths and polarizations. There is unfortunately no simple solution to this problem, but one possible strategy is to subtract only a fraction of the blank to compensate for the reduced sample transmission. In Figure 4b we have subtracted 87% of the blank background, which corresponds to the surface area fraction unoccupied by dimers in the SEM micrograph in Figure 1a. As mentioned in the Electrostatics Simulations Section, the experimental directivity ratios thus obtained, i.e., of the order 55 for the perpendicular and above 100 for parallel polarization configurations, respectively, are found to be in good agreement with theory. In Figure S2 in the Supporting Information, we also show how straylight reduction would significantly increase the sensitivity of hydrogen sensing experiments based on directional scattering, as expected. However, none of the data shown in Figures 1–3 have been subject to background subtraction.

Summary and Conclusions. We fabricated subwavelength Pd–Au dimer nanoantennas and found that they exhibited an extremely pronounced elastic scattering directionality. The experimental data were found to be in good agreement with electrostatics simulations. We also demonstrated that the nanoantennas could be used to sense hydrogen using a simple self-referenced single-wavelength optical detection scheme based on the directionality effect. In perspective, our findings indicate that the heterometallic approach to directional nanoantennas introduced earlier²⁰ is surprisingly robust with respect to the choice of metals. In fact, the basic concept is generic and can be applied to a wide range of materials, including dielectric and semiconductor antenna components. We believe that further exploration of these concepts could lead to a whole new class of directional nanoantennas and nanophotonic sensors with diverse and novel functionalities based on materials asymmetry.

■ ASSOCIATED CONTENT

Supporting Information

Figures with additional text and formulas. This material is available free of charge via the Internet at <http://pubs.acs.org>.

■ AUTHOR INFORMATION

Corresponding Author

*E-mail: mikael.kall@chalmers.se

Notes

The authors declare no competing financial interest.

■ ACKNOWLEDGMENTS

We would like to thank Dr. Vladimir Miljkovic for valuable discussions. Financial support from the Swedish Foundation for Strategic Research (project RMA08), the Swedish Research Council, and Göran Gustafsson Foundation is gratefully acknowledged.

■ REFERENCES

- (1) Schlapbach, L.; Zuttel, A. *Nature* **2001**, *414*, 353–358.
- (2) Fukai, Y. *The Metal-Hydrogen System*; Springer-Verlag: Berlin, Germany, 1993.
- (3) Vargas, W. E.; Rojas, I.; Azofeifa, D. E.; Clark, N. *Thin Solid Films* **2006**, *496*, 189–196.
- (4) Favier, F.; Walter, E. C.; Zach, M. P.; Benter, T.; Penner, R. M. *Science* **2001**, *293*, 2227–2231.
- (5) Zeng, X.-Q.; et al. *ACS Nano* **2011**, *5*, 7443–7452.
- (6) Larsson, E. M.; Langhammer, C.; Zorić, I.; Kasemo, B. *Science* **2009**, *326*, 1091–1094.
- (7) Shegai, T.; Langhammer, C. *Adv. Mater.* **2011**, *23*, 4409–4414.
- (8) Chadwick, B.; Tann, J.; Brungs, M.; Gal, M. *Sens. Actuators, B* **1994**, *17*, 215–220.
- (9) Gremaud, R.; et al. *Adv. Mater.* **2007**, *19*, 2813–+.
- (10) Liu, N.; Tang, M. L.; Hentschel, M.; Giessen, H.; Alivisatos, A. P. *Nat. Mater.* **2011**, *10*, 631–636.
- (11) Tittl, A.; et al. *Nano Lett.* **2011**, *11*, 4366–4369.
- (12) Giannini, V.; Fernández-Domínguez, A. I.; Heck, S. C.; Maier, S. A. *Chem. Rev.* **2011**, *111*, 3888–3912.
- (13) Halas, N. J.; Lal, S.; Chang, W.-S.; Link, S.; Nordlander, P. *Chem. Rev.* **2011**, *111*, 3913–3961.
- (14) Anker, J. N.; et al. *Nat. Mater.* **2008**, *7*, 442–453.
- (15) Svedendahl, M.; Chen, S.; Dmitriev, A.; Kall, M. *Nano Lett.* **2009**, *9*, 4428–4433.
- (16) Xu, H. X.; Kall, M. *Sens. Actuators, B* **2002**, *87*, 244–249.
- (17) Rindzevicius, T.; Alaverdyan, Y.; Kall, M.; Murray, W. A.; Barnes, W. L. *J. Phys. Chem. C* **2007**, *111*, 11806–11810.
- (18) Chen, S.; Svedendahl, M.; Duyne, R. P. V.; Käll, M. *Nano Lett.* **2011**, *11*, 1826–1830.
- (19) Homola, J.; Yee, S. S.; Gauglitz, G. *Sens. Actuators, B* **1999**, *54*, 3–15.
- (20) Shegai, T.; et al. *Nat. Commun.* **2011**, *2*, 481.
- (21) Fredriksson, H.; et al. *Adv. Mater.* **2007**, *19*, 4297–+.
- (22) Zoric, I.; Larsson, E. M.; Kasemo, B.; Langhammer, C. *Adv. Mater.* **2010**, *22*, 4628–4633.
- (23) Shegai, T.; Brian, B. r.; Miljković, V. D.; Käll, M. *ACS Nano* **2011**, *5*, 2036–2041.
- (24) Evlyukhin, A. B.; et al. *Nano Lett.* **2010**, *10*, 4571–4577.
- (25) Langhammer, C.; Zoric, I.; Kasemo, B. *Nano Lett.* **2007**, *7*, 3122–3127.
- (26) Johansson, P. *Phys. Rev. B* **2011**, *83*, 195408.
- (27) Martin, O. J. F.; Dereux, A.; Girard, C. *J. Opt. Soc. Am. A* **1994**, *11*, 1073–1080.
- (28) Johnson, P. B.; Christy, R. W. *Phys. Rev. B* **1972**, *6*, 4370–4379.
- (29) Palik, E. D. *Handbook of Optical Constants of Solids II*; Academic Press: Waltham, MA, 1999.
- (30) Langhammer, C.; Kasemo, B.; Zoric, I. *J. Chem. Phys.* **2007**, *126*, 194702.
- (31) Lukosz, W.; Kunz, R. E. *J. Opt. Soc. Am.* **1977**, *67*, 1607–1615.
- (32) Lukosz, W.; Kunz, R. E. *J. Opt. Soc. Am.* **1977**, *67*, 1615–1619.
- (33) Lieb, M. A.; Zavislan, J. M.; Novotny, L. *J. Opt. Soc. Am. B* **2004**, *21*, 1210–1215.
- (34) Shegai, T.; et al. *Nano Lett.* **2011**, *11*, 706–711.